LETTER

doi:10.1038/nature09682

Spin–orbit qubit in a semiconductor nanowire

S. Nadj-Perge[1]*, S. M. Frolov[1]*, E. P. A. M. Bakkers[1,2] & L. P. Kouwenhoven[1]

Motion of electrons can influence their spins through a fundamental effect called spin–orbit interaction. This interaction provides a way to control spins electrically and thus lies at the foundation of spintronics[1]. Even at the level of single electrons, the spin–orbit interaction has proven promising for coherent spin rotations[2]. Here we implement a spin–orbit quantum bit (qubit) in an indium arsenide nanowire, where the spin–orbit interaction is so strong that spin and motion can no longer be separated[3,4]. In this regime, we realize fast qubit rotations and universal single-qubit control using only electric fields; the qubits are hosted in single-electron quantum dots that are individually addressable. We enhance coherence by dynamically decoupling the qubits from the environment. Nanowires offer various advantages for quantum computing: they can serve as one-dimensional templates for scalable qubit registers, and it is possible to vary the material even during wire growth[5]. Such flexibility can be used to design wires with suppressed decoherence and to push semiconductor qubit fidelities towards error correction levels. Furthermore, electrical dots can be integrated with optical dots in p–n junction nanowires[6]. The coherence times achieved here are sufficient for the conversion of an electronic qubit into a photon, which can serve as a flying qubit for long-distance quantum communication.

Figure 1a shows a scanning electron microscope image of our nanowire device. Two electrodes, source and drain, are used to apply a voltage bias of 6 mV across the InAs nanowire. Voltages applied to five closely spaced, narrow gates underneath the nanowire create a confinement potential for two electrons separated by a tunnelling barrier. The defined structure is known as a double quantum dot in the (1, 1) charge configuration[7].

Each of the two electrons represents a spin–orbit qubit (Fig. 1b). In the presence of strong spin–orbit coupling, neither spin nor orbital number is separately well defined. Instead, each qubit state is a spin–orbit doublet, $\Uparrow$ and $\Downarrow$. Similar to pure spin states, a magnetic field, B, controls the energy splitting, $E_Z = g\mu_B B$, between spin–orbit states, where g is the Landé g-factor in a quantum dot and μ_B is the Bohr magneton. The crucial difference from a spin qubit is that in a spin–orbit qubit the orbital part of the spin–orbit wavefunction is used for qubit manipulation[2,8].

The qubit read-out and initialization rely on the effect of spin blockade[9,10]. A source–drain bias induces a current of electrons passing one by one through the double dot. The process of electron transfer between the dots can be allowed energetically but blocked by a spin selection rule. For instance, a (1, 1) triplet state cannot change into a (0, 2) singlet state. This stops the left-hand electron from tunnelling into the right-hand dot, and thereby blocks the current. In practice, the double dot becomes blocked only in a parallel configuration, that is, in either a ($\Uparrow$, $\Uparrow$) or a ($\Downarrow$, $\Downarrow$) state, because antiparallel states decay quickly to a non-blocked singlet state[11,12]. By idling the qubits in the parameter range of spin blockade, they will be initialized in one of the two parallel states with equal probability. We note that spin–orbit and hyperfine interactions also mediate a slower decay of parallel states into (0, 2)[7,9,10]. This reduces the read-out fidelity to 70–80% (Supplementary Information, section 5.1).

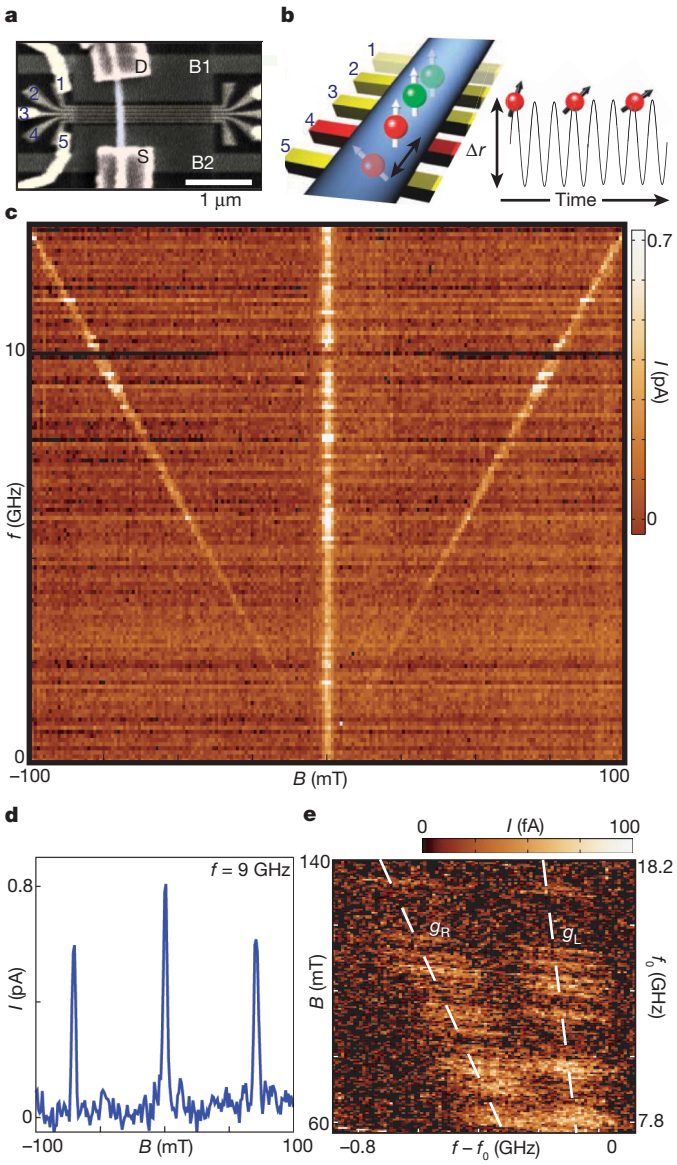

Figure 1 | Electric-dipole spin resonance. **a**, Scanning electron microscope image of a prototype device showing source (S) and drain (D) contacts, narrow gates one to five and wide gates B1 and B2. **b**, Left-hand (red) and right-hand (green) quantum dots are formed between gates two and five. A microwave electric field applied to gate four oscillates both electrons with amplitude $\sim\Delta r$, inducing EDSR. **c**, Spin blockade is lifted near $B = 0$ and on resonance when $f = g\mu_B B/h$. Here the microwave power is $P = -42$ dBm. I, current. **d**, Trace extracted from **c** at $f = 9$ GHz. **e**, Magnified view of the EDSR line, which is split at high B values owing to the difference between g_L and g_R. At each B value, the frequency is swept in a fixed range around $f_0 = g\mu_B B/h$ ($g = 9.28$). The current at resonance varies owing to non-monotonic microwave transmission.

[1]Kavli Institute of Nanoscience, Delft University of Technology, 2600 GA Delft, The Netherlands. [2]Department of Applied Physics, Eindhoven University of Technology, 5600 MB Eindhoven, The Netherlands.
*These authors contributed equally to this work.

A microwave-frequency electric field applied to gate four oscillates electrons inside the nanowire (Fig. 1b). This motion can induce resonant transitions between spin–orbit states by means of an effect called electric-dipole spin resonance[2,8,13–16] (EDSR). Such transitions are expected when the frequency of the a.c. electric field is equal to the Larmor frequency, $f_0 = g\mu_B B/h$ (h, Planck's constant). At resonance, the spin–orbit state of the double dot rapidly changes from parallel to antiparallel. The antiparallel state does not experience spin blockade, so the left-hand electron tunnels to the right, thereby contributing to the current. Figure 1c shows the resonance as a V shape that maps out the Larmor frequency in the plane of microwave frequency and magnetic field.

The V-shaped resonance signal vanishes in the vicinity of zero magnetic field. This behaviour is consistent with spin–orbit mediated EDSR: the effect of spin–orbit interaction must cancel at zero field owing to time-reversal symmetry[2,16]. The field-dependent EDSR strength rules out a.c. magnetic field and hyperfine field gradient as possible mechanisms. A g-tensor modulation in our nanowires is estimated to be too weak to drive EDSR (Supplementary Information, section 2). The current peak near zero magnetic field arises from the hyperfine interaction between electron spin and the nuclear spin bath[11,12]. From the width of this hyperfine-induced peak, we extract the root mean squared magnetic field generated by the fluctuating nuclear spins, $B_N = 0.66 \pm 0.1$ mT (ref. 17). The width of the EDSR line at low microwave power is also consistent with broadening due to fluctuating nuclear spins[18] (that is, the side EDSR peaks and the central hyperfine peak have comparable widths in Fig. 1d).

At higher magnetic field, the resonance line splits (Fig. 1e), indicating that the g-factors in the left- and right-hand dots, g_L and g_R, are different. This is expected for quantum dots of different sizes because confinement changes the effective g-factor[19]. We measured the confinement as the orbital excitation energy at the $(1,0) \leftrightarrow (0,1)$ transition and found 7.5 ± 0.1 meV for the left-hand dot and 9.0 ± 0.2 meV for the right-hand dot. A smaller orbital excitation energy should correspond to a larger g-factor in InAs; therefore, we assign the values obtained from Fig. 1e to the left- and right-hand dots as follows: $|g_L| = 9.2 \pm 0.1$ and $|g_R| = 8.9 \pm 0.1$. At frequencies above 10 GHz, the two resonances are more than a linewidth apart, allowing us to control the left- and right-hand qubits separately[8].

Coherent control over spin–orbit states is demonstrated in a time-resolved measurement of Rabi oscillations[2,18,20], explained in Fig. 2a, b. Periodic square pulses shift the relative positions of the energy levels in the two dots between spin blockade and Coulomb blockade. First, the double dot is initialized in a parallel state by idling in spin blockade. This is followed by a shift to Coulomb blockade, from which electrons cannot escape. While in Coulomb blockade, a resonant microwave burst is applied for a time τ_{burst} to induce qubit rotation. Finally, the double dot is brought back into spin blockade for read-out. At the read-out stage, the probability of the left-hand electron tunnelling out is proportional to the probability of projecting the final state onto the (1, 1) singlet. This cycle is repeated continuously.

The singlet component in the final state is measured as the d.c. current. The current oscillates as τ_{burst} is varied, reflecting Rabi oscillations of the driven qubit (Fig. 2c). Rabi oscillations are observed for driving frequencies in the range $f \approx 9$–19 GHz. Rabi oscillations are not observed at lower frequencies (and lower magnetic fields) because the effective spin–orbit field, B_{SO}, is less than B_N, such that nuclear fluctuations average out the coherent qubit dynamics. We note that the observation of incoherent EDSR (Fig. 1c) requires a much smaller B_{SO}, because even qubit rotations with a random phase contribute to extra current near resonance.

Our highest Rabi frequency is $f_R = 58 \pm 2$ MHz (Fig. 2d), achieved at $f = 13$ GHz. The field B_{SO} is expected to grow with B (ref. 16); however, at higher driving frequencies the Rabi frequency is limited by the maximum microwave source power and by the reduced transmission of the microwave circuit. With the strongest driving, the amplitude of the orbital oscillation is estimated to reach 1 nm. The qubit state is flipped in ~110 microwave periods, and thus rotated by ~1.6° per cycle of the orbital motion.

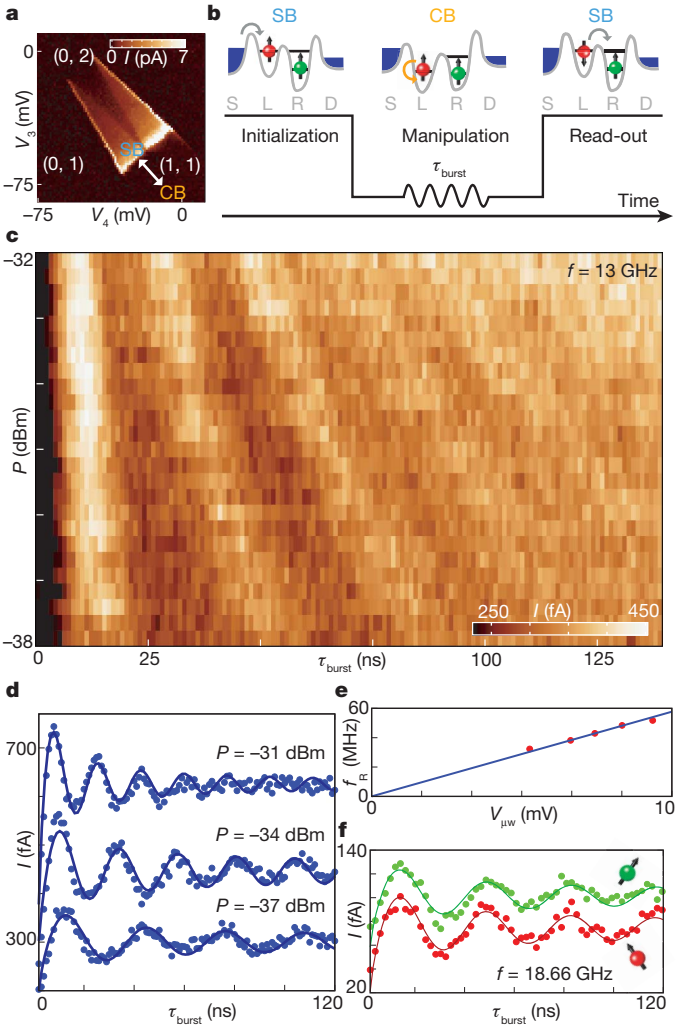

Figure 2 | Rabi oscillations. **a**, Charge stability diagram obtained by sweeping the voltages, V_3 and V_4, on gates three and four. CB, Coulomb blockade; SB, spin blockade. **b**, Measurement cycle with diagrams showing electrochemical potentials of the source (S), drain (D), left-hand dot (L) and right-hand dot (R) for each stage. **c**, Rabi oscillations for a range of microwave powers at $f = 13$ GHz and $B = 102$ mT. **d**, Rabi oscillations at $f = 13$ GHz, with fits to[21] $a\cos(f_R\tau_{burst} + \varphi)/\tau^d + b$ ($d = 0.8$ for top trace and $d = 0.5$ for the bottom two traces). Rabi frequencies are 58 ± 2, 43 ± 2 and 32 ± 2 MHz (top to bottom). Linear slopes of 2 fA ns^{-1}, 1 fA ns^{-1} and 0.3 fA ns^{-1} (top to bottom) are subtracted to flatten the average. They are attributed to photon-assisted tunnelling. Traces are offset vertically for clarity. **e**, Dependence of f_R on driving amplitude, $V_{\mu w} = 2(P \times 50\,\Omega)^{0.5}$, with a linear fit. **f**, Rabi oscillations with separated addressing of the left- and right-hand qubits at $f = 18.66$ GHz and $B = 144$ mT (red) and 149 mT (green), with $f_R = 29 \pm 2$ MHz fitted to the expression used in **d**.

We can resolve up to five Rabi oscillation periods. The damping of the oscillations at a microwave power of $P < -32$ dBm is consistent with a $\sim\tau_{burst}^{-0.5}$ decay envelope observed previously for rotations of a single spin interacting with a slow nuclear bath[21]. We have verified that the relaxation time, T_1, does not limit coherent evolution on timescales up to 1 μs (Supplementary Information, section 3). The qubit manipulation fidelity is $48 \pm 2\%$, estimated by comparing the values of B_{SO} and B_N (ref. 18; Supplementary Information, section 5.3). As expected, the Rabi frequency is proportional to the square root of the microwave power, P, applied to the gate (Fig. 2e). Absorption of microwave photons allows interdot tunnelling regardless of the qubit state. This

effect probably accelerates the decay of Rabi oscillations near the highest power[2,18] (Fig. 2d, top trace). However, the apparent photon-assisted tunnelling is substantially reduced for $P < -32$ dBm, although Rabi frequencies remain high.

In Fig. 2c, d only the left qubit is rotated. Figure 2f shows data from coherent rotations of either the left- or the right-hand qubit induced at the same microwave frequency but at two different magnetic fields, which correspond to the two EDSR resonance conditions shown in Fig. 1e (ref. 22; Supplementary information, section 4).

In the Rabi experiment, the qubit state is rotated around only one axis. This is not enough for full qubit operation, which ultimately requires the preparation of an arbitrary superposition of $\Uparrow$ and $\Downarrow$, known as universal control[23–25]. Such ability is demonstrated in a Ramsey experiment (Fig. 3a, b). Here two short bursts with different microwave phases are applied during the manipulation stage. In the reference frame that rotates at the Larmor frequency, the qubit is initially rotated from $|+z\rangle$ to $|-y\rangle$ on the Bloch sphere by applying a $\pi/2$ rotation around the x axis. After a delay time, τ, we apply a $3\pi/2$ pulse. The tunable phase of the microwave signal, ϕ, sets the axis of the second rotation ($\phi = 0$ corresponds to a rotation around x and $\phi = \pi/2$ corresponds to a rotation around y). The final z component depends on the axis of the second rotation as well as on dephasing. The double-dot current oscillates with ϕ, revealing Ramsey fringes (Fig. 3a). The contrast of the Ramsey fringes decreases with increasing τ, allowing us to determine the inhomogeneous dephasing time, $T_2^* = 8 \pm 1$ ns (Fig. 3b).

Coherence can be extended by a Hahn echo technique, which partly cancels dephasing coming from a slowly varying nuclear magnetic field (Fig. 3c, d). In the echo sequence, a π pulse is applied halfway between the two $\pi/2$ pulses. The contrast of the Ramsey fringes is

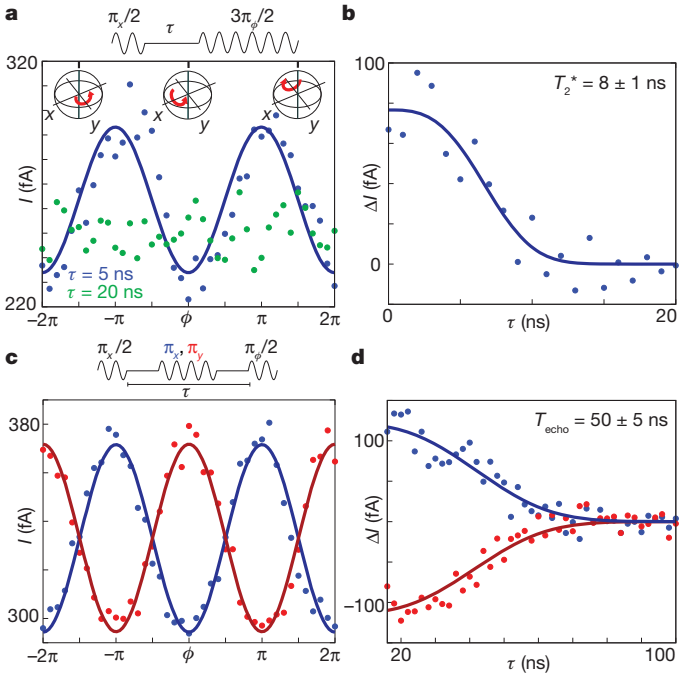

Figure 3 | Universal qubit control and coherence times. **a**, Ramsey experiment sequence (top) and measurement of fringes $I(\phi)$ for $\tau = 5$ and 20 ns. The axes of the second rotation are indicated with red arrows on the Bloch spheres for three values of ϕ. **b**, Decay of the Ramsey fringe contrast, $\Delta I = I(\phi = \pi) - I(\phi = 0)$, fitted to $\exp[-(\tau/T_2^*)^2]$. **c**, Hahn echo sequence (top) extends fringe contrast beyond $\tau = 34$ ns. Fringes for two orthogonal phases of the π pulse (π_x, blue; π_y, red) are out of phase. **d**, Decay of the fringe contrast obtained for the two Hahn echo sequences (π_x, blue; π_y, red) is used to extract T_{echo} from a fit to $\exp[-(\tau/T_{echo})^3]$. A fit to $\exp[-(\tau/T_{echo})^4]$ gives a similar value of T_{echo}. In this figure, the duration of a π pulse is 14 ns, with $P = -35$ dBm, $f = 13$ GHz and $B = 102$ mT.

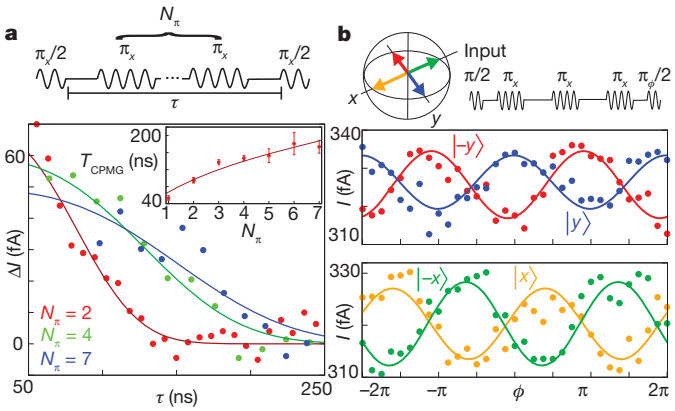

Figure 4 | Dynamical decoupling. **a**, Decay of the contrast of the Ramsey fringes for CPMG sequences (top) with an increasing number of π pulses, N_π. Solid lines are fits to $\exp[-(\tau/T_{CPMG})^3]$. Inset, coherence times T_{CPMG} versus N_π are fitted to N_π^d with $d = 0.53 \pm 0.1$. Error bars are standard deviations of $\Delta I(\tau)$ fits. **b**, Ramsey fringes for four different phases of the initial $\pi/2$ pulse obtained for an $N_\pi = 3$ CPMG sequence (shown above the panel) with $\tau = 150$ ns. The input states are indicated with arrows on the Bloch sphere. In this figure, the duration of a π pulse is 8 ns with $P = -32$ dBm, $f = 13$ GHz and $B = 102$ mT.

extended to longer coherent evolution times by performing Hahn echo (Fig. 3c). The phase of the fringes can be flipped depending on whether the π rotation is around the x axis (π_x) or around the y axis (π_y). Hahn echoes of both these types increase the coherence time to $T_{echo} = 50 \pm 5$ ns (Fig. 3d).

Gate-defined spin qubits were previously only realized in lateral quantum dots in GaAs–AlGaAs two-dimensional electron gases[9]. Owing to the much stronger spin–orbit interaction in InAs, the Rabi frequencies in our nanowire spin–orbit qubits are more than an order of magnitude higher than in GaAs dots[2]. Dephasing times, T_2^*, are of the same order in InAs and GaAs quantum dots[23,26]. The relatively low T_{echo} found in the present work encourages further study. A likely reason is faster nuclear spin fluctuations caused by the large nuclear spin of indium, $I = 9/2$. However, charge noise and nearby paramagnetic impurities cannot be ruled out as significant dephasing sources (Supplementary Information, section 6). Nanowires offer future solutions for suppressing the effects of nuclear spins, such as nanowires with sections of nuclear-spin-free silicon. The qubit can be stored in a silicon section of the nanowire and moved to an InAs section only for manipulation using spin–orbit interaction.

In the present qubit, longer coherence times can already be achieved by Carr–Purcell–Meiboom–Gill (CPMG) dynamical-decoupling pulse sequences[27,28] (Fig. 4a). Here a single echo π pulse is replaced with an array of equidistant π pulses, each of which refocuses the qubit state. The total time of coherent evolution grows as the number of π pulses is increased (Fig. 4a, inset). Importantly, an arbitrarily prepared qubit state in the x–y plane is preserved during the decoupling sequence. This is verified in Fig. 4b, which shows that the phase of the initial $\pi/2$ pulse determines the phase of the Ramsey fringes. Similar evaluation was carried out for CPMG sequences of up to seven π pulses. In future, more efficient dynamical decoupling can be achieved using nuclear spin state preparation[27,29] in combination with faster π pulses or adiabatic pulse techniques[30].

METHODS SUMMARY

We fabricate devices on undoped silicon substrates. Instead of a global back gate, two wide gates, B1 and B2, are located underneath the nanowire contacts (Fig. 1a). They are set to constant positive voltages to enhance conductance through the nanowire. The wide gates are covered by a 50-nm layer of Si_3N_4 dielectric; on top of this layer narrow gates and a 25-nm layer of Si_3N_4 are deposited. InAs nanowires with diameters between 50 and 80 nm are grown nearly free of stacking faults using metal-organic vapour phase epitaxy. The wires have the wurtzite crystal symmetry

with the *c* axis along the long nanowire axis. Nanowires are transferred in air from the mother chip to the device substrates, which already contain Ti–Au gates. Selected wires are contacted with ohmic Ti–Al electrodes, and during the same step contacts are made to the gates. We make measurements in a He^3 refrigerator at $T = 300$ mK. A magnetic field is applied in the plane of the substrate at an angle of $45^\circ \pm 5^\circ$ with respect to the nanowire. We create high-frequency pulses using two arbitrary waveform generators (one gigasample per second) and a 20-GHz, 23-dBm microwave vector source. Pulses are delivered to the sample through silver-plated CuNi coaxial lines with 36-dB attenuators followed by coplanar striplines printed on the sample holder. Square pulses are applied synchronously to gates two and four. Microwave bursts are applied to gate four. A measurement cycle lasts 2 μs in the coherent rotations detailed in Fig. 2f. In the rest of the paper, a cycle lasts 600 ns and each data point is averaged over 5–40 million cycles. The pulse period should remain less than 2 μs to detect the double-dot current, which is limited by the noise floor of the d.c. current amplifier.

Received 29 September; accepted 10 November 2010.

1. Datta, S. & Das, B. Electronic analog of the electrooptic modulator. *Appl. Phys. Lett.* **56,** 665–667 (1990).
2. Nowack, K. C., Koppens, F. H. L., Nazarov, Y. V. & Vandersypen, L. M. K. Coherent control of a single electron spin with electric fields. *Science* **318,** 1430–1433 (2007).
3. Fasth, C., Fuhrer, A., Samuelson, L., Golovach, V. N. & Loss, D. Direct measurement of the spin-orbit interaction in a two-electron InAs nanowire quantum dot. *Phys. Rev. Lett.* **98,** 266801 (2007).
4. Pfund, A., Shorubalko, I., Ensslin, K. & Leturcq, R. Spin-state mixing in InAs double quantum dots. *Phys. Rev. B* **76,** 161308 (2007).
5. Minot, E. D. *et al.* Single quantum dot nanowire LEDs. *Nano Lett.* **7,** 367–371 (2007).
6. van Weert, M. H. M. *et al.* Selective excitation and detection of spin states in a single nanowire quantum dot. *Nano Lett.* **9,** 1989–1993 (2009).
7. Nadj-Perge, S. *et al.* Disentangling the effects of spin-orbit and hyperfine interactions on spin blockade. *Phys. Rev. B* **81,** 201305 (2010).
8. Pioro-Ladriere, M. *et al.* Electrically driven single-electron spin resonance in a slanting Zeeman field. *Nature Phys.* **4,** 776–779 (2008).
9. Hanson, R., Kouwenhoven, L. P., Petta, J. R., Tarucha, S. & Vandersypen, L. M. K. Spins in few-electron quantum dots. *Rev. Mod. Phys.* **79,** 1217–1265 (2007).
10. Pfund, A., Shorubalko, I., Ensslin, K. & Leturcq, R. Suppression of spin relaxation in an InAs nanowire double quantum dot. *Phys. Rev. Lett.* **99,** 036801 (2007).
11. Koppens, F. H. L. *et al.* Control and detection of singlet-triplet mixing in a random nuclear field. *Science* **309,** 1346–1350 (2005).
12. Johnson, A. C. *et al.* Triplet-singlet spin relaxation via nuclei in a double quantum dot. *Nature* **435,** 925–928 (2005).
13. Rashba, E. I. & Efros, A. L. Orbital mechanisms of electron-spin manipulation by an electric field. *Phys. Rev. Lett.* **91,** 126405 (2003).
14. Kato, Y. *et al.* Gigahertz electron spin manipulation using voltage-controlled *g*-tensor modulation. *Science* **299,** 1201–1204 (2003).
15. Laird, E. A. *et al.* Hyperfine-mediated gate-driven electron spin resonance. *Phys. Rev. Lett.* **99,** 246601 (2007).
16. Golovach, V. N., Borhani, M. & Loss, D. Electric-dipole-induced spin resonance in quantum dots. *Phys. Rev. B* **74,** 165319 (2006).
17. Danon, J. & Nazarov, Y. V. Pauli spin blockade in the presence of strong spin-orbit coupling. *Phys. Rev. B* **80,** 041301 (2009).
18. Koppens, F. H. L. *et al.* Driven coherent oscillations of a single electron spin in a quantum dot. *Nature* **442,** 766–771 (2006).
19. Pryor, C. E. & Flatte, M. E. Lande *g* factors and orbital momentum quenching in semiconductor quantum dots. *Phys. Rev. Lett.* **96,** 026804 (2006).
20. Berezovsky, J., Mikkelsen, M. H., Stoltz, N. G., Coldren, L. A. & Awschalom, D. D. Picosecond coherent optical manipulation of a single electron spin in a quantum dot. *Science* **320,** 349–352 (2008).
21. Koppens, F. H. L. *et al.* Universal phase shift and nonexponential decay of driven single-spin oscillations. *Phys. Rev. Lett.* **99,** 106803 (2007).
22. Obata, T. *et al.* Coherent manipulation of individual electron spin in a double quantum dot integrated with a micromagnet. *Phys. Rev. B* **81,** 085317 (2010).
23. Koppens, F. H. L., Nowack, K. C. & Vandersypen, L. M. K. Spin echo of a single electron spin in a quantum dot. *Phys. Rev. Lett.* **100,** 236802 (2008).
24. Press, D., Ladd, T. D., Zhang, B. Y. & Yamamoto, Y. Complete quantum control of a single quantum dot spin using ultrafast optical pulses. *Nature* **456,** 218–221 (2008).
25. Foletti, S., Bluhm, H., Mahalu, D., Umansky, V. & Yacoby, A. Universal quantum control of two-electron spin quantum bits using dynamic nuclear polarization. *Nature Phys.* **5,** 903–908 (2009).
26. Petta, J. R. *et al.* Coherent manipulation of coupled electron spins in semiconductor quantum dots. *Science* **309,** 2180–2184 (2005).
27. Bluhm, H. *et al.* Long coherence of electron spins coupled to a nuclear spin bath. Preprint at ⟨http://arxiv.org/abs/1005.2995⟩ (2010).
28. Barthel, C., Medford, J., Marcus, C. M., Hanson, M. P. & Gossard, A. C. Interlaced dynamical decoupling and coherent operation of a singlet-triplet qubit. Preprint at ⟨http://arxiv.org/abs/1007.4255⟩ (2010).
29. Reilly, D. J. *et al.* Suppressing spin qubit dephasing by nuclear state preparation. *Science* **321,** 817–821 (2008).
30. Fuchs, G. D., Dobrovitski, V. V., Toyli, D. M., Heremans, F. J. & Awschalom, D. D. Gigahertz dynamics of a strongly driven single quantum spin. *Science* **326,** 1520–1522 (2009).

Supplementary Information is linked to the online version of the paper at www.nature.com/nature.

Acknowledgements We thank K. Nowack, R. Schouten, M. Laforest, K. Zuo, M. Hocevar, R. Algra, J. van Tilburg, M. Scheffler, G. de Lange, V. Dobrovitski, J. Danon, R. Hanson, R. Liu, Yu. V. Nazarov and L. Vandersypen for their help. This work has been supported by NWO/FOM (the Netherlands Organization for Scientific Research), an ERC Advanced Grant and through the DARPA program QUEST.

Author Contributions S.N.-P., S.M.F. and L.P.K. designed the experiments. S.N.-P. and S.M.F. performed the measurements and analysed the data. E.P.A.M.B. provided nanowires. All authors wrote the manuscript.

Author Information Reprints and permissions information is available at www.nature.com/reprints. The authors declare no competing financial interests. Readers are welcome to comment on the online version of this article at www.nature.com/nature. Correspondence and requests for materials should be addressed to L.P.K. (l.p.kouwenhoven@tudelft.nl).